LETTER

https://doi.org/10.1038/s41586-019-1421-y

Quantum-enhanced sensing of a single-ion mechanical oscillator

Katherine C. McCormick[1,2]*, Jonas Keller[1], Shaun C. Burd[1,2], David J. Wineland[1,2,3], Andrew C. Wilson[1] & Dietrich Leibfried[1]

Special quantum states are used in metrology to achieve sensitivities below the limits established by classically behaving states[1,2]. In bosonic interferometers, squeezed states[3], number states[4,5] and 'Schrödinger cat' states[5] have been implemented on various platforms and have demonstrated improved measurement precision over interferometers using coherent states[6,7]. Another metrologically useful state is an equal superposition of two eigenstates with maximally different energies; this state ideally reaches the full interferometric sensitivity allowed by quantum mechanics[8,9]. Here we demonstrate the enhanced sensitivity of these quantum states in the case of a harmonic oscillator. We extend an existing experimental technique[10] to create number states of order up to $n = 100$ and to generate superpositions of a harmonic oscillator ground state and a number state of the form $\frac{1}{\sqrt{2}}(|0\rangle + |n\rangle)$ with n up to 18 in the motion of a single trapped ion. Although experimental imperfections prevent us from reaching the ideal Heisenberg limit, we observe enhanced sensitivity to changes in the frequency of the mechanical oscillator. This sensitivity initially increases linearly with n and reaches a maximum at $n = 12$, where we observe a metrological enhancement of 6.4(4) decibels (the uncertainty is one standard deviation of the mean) compared to an ideal measurement on a coherent state with the same average occupation number. Such measurements should provide improved characterization of motional decoherence, which is an important source of error in quantum information processing with trapped ions[11,12]. It should also be possible to use the quantum advantage from number-state superpositions to achieve precision measurements in other harmonic oscillator systems.

A large variety of experimental systems—including optical and microwave[5,13] resonators, micro-mechanical oscillators[14] and the motion of trapped neutral atoms[15] and ions[16]—can be modelled as harmonic oscillators and controlled in the quantum regime. This opens the possibility of designing and generating advantageous harmonic oscillator quantum states to increase sensitivity or speed when characterizing or controlling the properties of these oscillators. Precisely controlled harmonic oscillators are crucial for precision metrology[17], fundamental quantum mechanical research[5] and quantum information processing[18].

The motion of a single atom in a typical trap constitutes a simple mechanical harmonic oscillator. This oscillator can be coupled to internal levels of the atom with electromagnetic fields to 'cool' its motion and transfer motional state information into electronic levels that can be read out by state-selective fluorescence[16]. Ion motional frequencies have been determined previously by resolved-sideband spectroscopy[16] and by excitation with oscillating[19] or pulsed[20,21] electric fields. The sensitivity to excitation by an oscillating electric field (often called a 'tickle') can be enhanced by first cooling the motion to the ground state and then detecting small increases in motional energy by exciting red sideband transitions that are energetically forbidden when the ion is in the ground state[22]. Here we implement an alternative approach for characterizing motional frequencies that is based on the interference of non-classical number-state superpositions[23]. These techniques can be especially useful for quantum information processing with trapped-ion systems[24], where qubits are coupled through shared modes of motion. The high fidelity required for fault-tolerant processing makes the stability of the harmonic motion of trapped ions a ubiquitous concern[11,12], particularly as experiments move towards miniaturized traps with smaller ion-to-electrode distances, exposing the ions' motion to larger stray electric fields and increased noise originating from the electrodes[25].

The interferometric sensitivity of superpositions of eigenstates depends on the difference in energy between the two states—in the experiments presented here, where the first state of the superposition is the ground state this energy difference scales linearly with n. Here, the harmonic oscillator number operator acts on the number states $|n\rangle$, giving $\hat{a}^\dagger\hat{a}\ |n\rangle = n\ |n\rangle$, where $\hat{a}$ is the annihilation ladder operator and $n \geq 0$ is an integer. We consider a harmonic oscillator with an oscillation frequency of $\omega + \delta\omega(t)$, where $\delta\omega(t)$ is a small, time-dependent correction due to noise and drift relative to the frequency ω of an ideal reference oscillator, which we call a local oscillator, in keeping with common terminology. We implement a Ramsey-type experiment, where the first effective $\pi/2$ pulse creates the state $|\Psi_n\rangle = \frac{1}{\sqrt{2}}(|0\rangle + |n\rangle)$, where n denotes the order of the state and the interferometer (in the following we omit normalization). In a frame rotating at the local oscillator frequency, $|0\rangle$ and $|n\rangle$ will acquire a relative phase between the two states that is proportional to n and to the integral of the fluctuations $\delta\omega(t)$ over time T. After a duration of T the state is

$$|\Psi_n\rangle_T = |0\rangle + \mathrm{e}^{in\phi}|n\rangle$$
$$\phi = -\int_0^T \delta\omega(t)\mathrm{d}t \quad (1)$$

Subsequently, a second effective $\pi/2$ pulse synchronous with the local oscillator recombines the number-state superposition to the ground state if $n\phi = (2m+1)\pi$ or to $|n\rangle$ if $n\phi = 2m\pi$, with m an integer. For a general ϕ, the final state (up to a global phase) is $|\Psi_n\rangle_f = \cos(n\phi/2)|n\rangle - i\sin(n\phi/2)|0\rangle$, with the probability of being in the ground state given by

$$P_0 = \frac{1}{2}[1-\cos(n\phi)] \quad (2)$$

To characterize the harmonic oscillator using interferometric measurements, we want to determine small deviations of ϕ around a nominal value with maximal sensitivity. This occurs when the slope $|\partial P_0/\partial\phi| = |(n/2)\sin(n\phi)| = n/2$, namely, when $n\phi \approx m\pi/2$, with m an odd integer ($m = \pm 1$ in the tracking experiments described below). We want to minimize

$$\delta\phi = \frac{\Delta P_0}{|\partial P_0/\partial\phi|} \quad (3)$$

[1]National Institute of Standards and Technology, Boulder, CO, USA. [2]Department of Physics, University of Colorado, Boulder, CO, USA. [3]Department of Physics, University of Oregon, Eugene, OR, USA. *e-mail: katherine.mccormick-1@colorado.edu

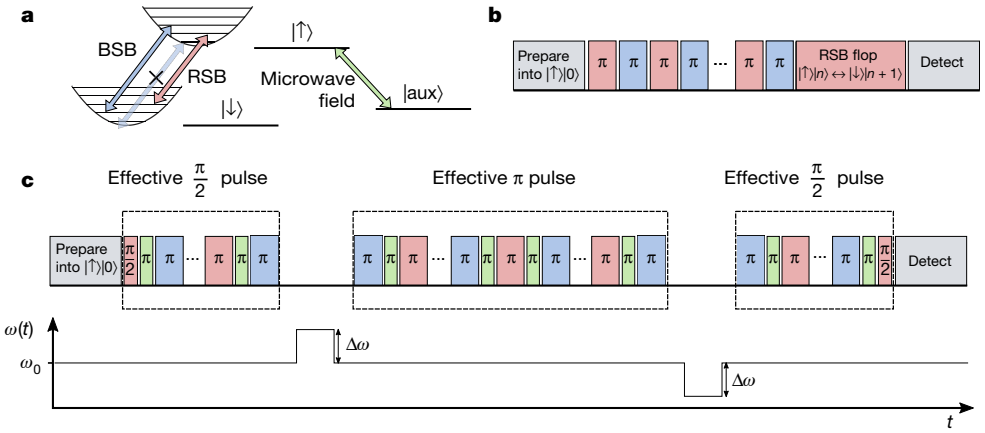

Fig. 1 | Generating number states and number-state superpositions. **a**, Relevant energy levels and transitions for the creation of motional states. BSB pulses transfer population between $|{\downarrow}\rangle\ |k\rangle$ and $|{\uparrow}\rangle\ |k+1\rangle$, whereas RSB pulses transfer population between $|{\uparrow}\rangle\ |k\rangle$ and $|{\downarrow}\rangle\ |k+1\rangle$. The BSB does not couple to $|{\uparrow}\rangle\ |0\rangle$ (crossed-out, faded blue arrow) because there is no energy level below the ground state. Transitions between the states $|{\uparrow}\rangle$ and $|\mathrm{aux}\rangle$ are driven by a microwave field (indicated in green), which does not change k. **b**, Pulse sequence for generating a harmonic oscillator number state. Alternating RSB and BSB π pulses are applied, with each pulse adding one quantum of motion (or more quanta on higher-order sidebands; see the main text) and flipping the spin of the state. To analyse the resulting state, an RSB pulse is applied for a variable duration (labelled 'RSB flop') and the final spin state is detected via state-selective fluorescence. **c**, Pulse sequences and trap frequencies for number-state interferometers. The first effective π/2 pulse creates $|0\rangle + |n\rangle$, followed by a free-precession period during which the mode frequency is increased by $\Delta\omega$. An effective π pulse swaps the phase of the superposition, $|0\rangle + \mathrm{e}^{i\phi}\ |n\rangle \rightarrow \mathrm{e}^{i\phi}\ |0\rangle + |n\rangle$. After another free-precession period with the mode frequency reduced by $\Delta\omega$, a final effective π/2 pulse closes the interferometer. For the composition of effective pulses see the main text.

where $\Delta P_0 = \sqrt{\langle P_0^2\rangle - \langle P_0\rangle^2}$ is the standard deviation of a population measurement that can discriminate between $|0\rangle$ and $|n\rangle$. Ideally, the measurement is projection noise limited[26], which implies $\Delta P_0 = \sqrt{P_0(1-P_0)}$. In this case, $\Delta P_0 = 1/2$ and $\delta\phi = 1/n$, which is the Heisenberg limit and can only be reached with non-classical oscillator states. In fact, the state $|0\rangle + |n\rangle$ satisfies the Margolus–Levitin bound for the maximal rate of evolution[8], implying that no other combination of states with quantum numbers between 0 and n can produce interference fringes with higher sensitivity to motional frequency changes. (Without the restriction of using quantum numbers only up to n, a Schrödinger cat state with an average occupation of n would also allow sensing with the same scaling as the $|0\rangle + |n\rangle$ superposition. This sensitivity is demonstrated approximately in a different form of interferometer, in which the motional states are entangled with the internal states, as described in ref. [27]). The phase uncertainty of classically behaving interferometers, which we define as those that use coherent oscillator states of the same average excitation number $\bar{n} = n/2$ and measurements of the oscillator energy (equivalent to the mean occupation number), will reduce only as $\delta\phi_{\mathrm{class}} = \sqrt{1/n}$ (see Methods).

In practice, the effective π/2 pulses will not have perfect fidelity and there will be added noise above the fundamental projection noise. Such imperfections reduce the contrast C ($0 \le C \le 1$) from the ideal value of $C = 1$, which can be incorporated as $P_0 = (C/2)[1-\cos(n\phi)]$. In our experiments, C decreases as the complexity of preparing superpositions increases with larger n. Additionally, because a single experiment gives us only one bit of information (the ion is determined to be in either $|0\rangle$ or $|n\rangle$), we need to perform multiple experiments to accumulate statistics to determine a phase shift. If the mode-frequency noise is not stable over the time period required to acquire statistics, then the contrast of our interferometer is reduced. This becomes more of a problem with higher-order interferometers because the susceptibility to mode-frequency noise increases with n. This limits the measurable gains in sensitivity to $n \le 12$ in our experimental setting (see below).

Experiments were performed with a single $^9\mathrm{Be}^+$ ion trapped 40 μm above a cryogenic (about 4 K) linear surface-electrode trap described elsewhere[28]. Improvements made to the experimental setup since the technique was initially demonstrated in ref. [10] are described in Methods. We use three levels within the electronic $^2\mathrm{S}_{1/2}$ ground-state hyperfine manifold, $|F=1, m_F=-1\rangle = |{\uparrow}\rangle$, $|F=2, m_F=-2\rangle = |{\downarrow}\rangle$ and $|F=2, m_F=0\rangle = |\mathrm{aux}\rangle$, to prepare approximate pure number states and number-state superpositions. Here, F is the total angular momentum and m_F is its component along the quantization axis, defined by a 1.43-mT static magnetic field. The states $|{\downarrow}\rangle$ and $|\mathrm{aux}\rangle$ are shifted from $|{\uparrow}\rangle$ by $\omega_0 \approx 2\pi \times (-1.281\ \mathrm{GHz})$ and $\omega_{\mathrm{aux}} \approx 2\pi \times (-1.261\ \mathrm{GHz})$, respectively (Fig. 1a). The non-classical motional states are created on the lowest-frequency (axial) mode of the three orthogonal harmonic oscillator modes of the ion, with frequency $\omega \approx 2\pi \times (7.2\ \mathrm{MHz})$. The ion is prepared in $|{\downarrow}\rangle\ |0\rangle$ with a fidelity exceeding 0.99 by Doppler laser cooling, followed by ground-state cooling[16,29] (the two transverse modes are only Doppler cooled to $\bar{n} < 1$. Sideband transitions from intermediate number state k $|{\downarrow}\rangle\ |k\rangle \leftrightarrow |{\uparrow}\rangle\ |k\pm1\rangle$ are implemented with stimulated Raman transitions from two photons that are detuned from the $^2\mathrm{S}_{1/2} \rightarrow {}^2\mathrm{P}_{1/2}$ transition (wavelength $\lambda \approx 313$ nm) by approximately +80 GHz (ref. [29]). Carrier transitions $|{\downarrow}\rangle\ |k\rangle \leftrightarrow |{\uparrow}\rangle\ |k\rangle$ and $|{\downarrow}\rangle\ |k\rangle \leftrightarrow |\mathrm{aux}\rangle\ |k\rangle$ are driven by microwave fields induced by a current through one of the surface-trap electrodes.

We can distinguish measurements of the $|{\uparrow}\rangle$ and $|{\downarrow}\rangle$ states with state-selective fluorescence[16]. When scattering light from a laser beam resonant with the $|{\downarrow}\rangle \leftrightarrow |\mathrm{P}_{3/2}, F=3, m_F=-3\rangle$ cycling transition, 14 to 16 photons are detected on average over 400 μs with a photomultiplier if the ion is in $|{\downarrow}\rangle$, whereas only 0.1 to 0.3 photons (dark counts and stray light) are detected on average if the ion is projected into $|{\uparrow}\rangle$. We identify outcomes of three or more counts with a measurement outcome of $|{\downarrow}\rangle$. Despite deviations from ideal Poisson statistics due to pumping into other hyperfine levels, histograms composed of many detections on an ion prepared in either $|{\downarrow}\rangle$ or $|{\uparrow}\rangle$ reveal discrimination errors below 0.02. After preparing $|{\downarrow}\rangle \rightarrow |{\uparrow}\rangle + |{\downarrow}\rangle$, we observe in $|{\downarrow}\rangle$ an average population of 0.489(4) and a variance of 0.249(2), close to the ideal values of 1/2 and 1/4. All stated uncertainties and error bars in the figures represent one standard deviation of the mean.

Starting from $|{\downarrow}\rangle\ |0\rangle$, the generation of higher-number states is accomplished by first applying a microwave π pulse to transform the initial state to $|{\uparrow}\rangle\ |0\rangle$, followed by a series of alternating red ($|{\uparrow}\rangle\ |k\rangle \rightarrow |{\downarrow}\rangle\ |k+1\rangle$; RSB) and blue ($|{\downarrow}\rangle\ |k\rangle \rightarrow |{\uparrow}\rangle\ |k+1\rangle$; BSB) sideband π pulses at frequencies $\omega_0 - \omega$ and $\omega_0 + \omega$, respectively, so that each pulse flips the spin of the internal state and adds a quantum of motion[10] (Fig. 1a, b). In general, we can use sidebands of order l at frequencies $\omega_0 - l\omega$ and $\omega_0 + l\omega$ to add l quanta of motion with a single π pulse. Whereas the Rabi frequencies of higher-order sidebands on a mode with a Lamb–Dicke parameter of $\eta < 1$ are suppressed by η^l near

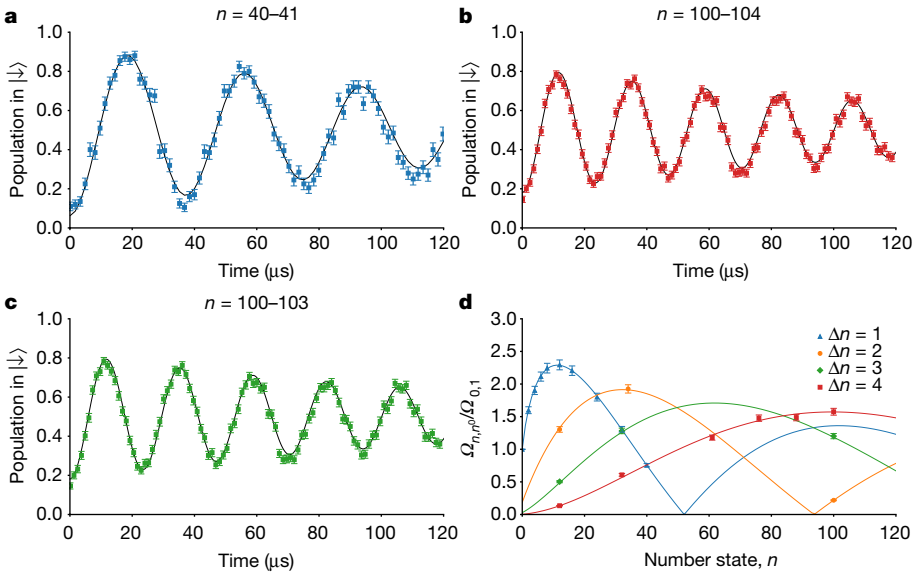

Fig. 2 | Sideband flopping on number states. a, RSB flopping on the first-order sideband of an $|\uparrow\rangle\ |n=40\rangle$ state prepared using first-order RSB and BSB pulses. The curve shows the probability of measuring $|\downarrow\rangle$ as a function of pulse duration during first-order RSB flopping to $|\downarrow\rangle\ |n=41\rangle$. Each point represents an average over 200 experiments. The error bars represent one standard deviation of the mean. Solid black lines show theory fits to the data, with the Rabi frequency, the initial contrast and an exponential decay constant as fit parameters. **b**, RSB flopping on the fourth-order sideband of $|\uparrow\rangle\ |n=100\rangle$. The curve shows the probability of measuring $|\downarrow\rangle$ as a function of pulse duration during fourth-order RSB flopping to $|\downarrow\rangle\ |n=104\rangle$. Each point represents an average over 500 experiments. **c**, Same as **b**, but on the third-order sideband of $|\uparrow\rangle\ |n=100\rangle \leftrightarrow |\downarrow\rangle\ |n=103\rangle$. **d**, First- to fourth-order sideband Rabi frequencies. All first-order data points (blue triangles) are fitted to determine the Lamb–Dicke parameter $\eta = 0.2632(2)$. Curves for higher-order sidebands are plotted for the same η. Measured Rabi frequencies for higher-order sidebands (symbols) are consistent with theory (solid lines) for all orders. The duration of the π pulse from $|n=0\rangle$ to $|n=1\rangle$ is approximately 13 μs; the pulse durations required to produce higher-number states can be calculated on the basis of this result and the plotted Rabi frequencies for higher-number states (see Methods).

the ground state, for higher-number states, the Rabi frequencies can be much larger than that of the first-order sideband[16] (see Fig. 2d).

We demonstrate control over the motional state of the ion by preparing it in different (approximately pure) number states and by Rabi-flopping on RSBs to determine the contrast, decay and n-dependent Rabi frequency[16] (see Fig. 2a). With the use of only first-order sidebands to create $|\uparrow\rangle\ |n=40\rangle$, we achieve RSB flopping ($|\uparrow\rangle\ |n=40\rangle \leftrightarrow |\downarrow\rangle\ |n=41\rangle$) with contrast greater than 70%. If we use up to fourth-order sidebands to create the motional state, we observe approximately 50% contrast when we flop $|n=100\rangle$ on the fourth-order RSB (Fig. 2 b). To verify that the population participating in the fourth-sideband flopping is in the desired number state, we also flop on the second- and third-order sidebands (Fig. 2c), which have distinctly different Rabi frequencies, and compare the Rabi frequencies of second- to fourth-order flopping to theory (coloured symbols in Fig. 2d). For the second sideband, we measure a Rabi frequency (in units of $\Omega_{0,1}$, the Rabi frequency of the $|n=0\rangle \leftrightarrow |n=1\rangle$ transition) of 0.2183 ± 0.008 for $n = 100$, which agrees with theory within one standard deviation. The calculated Rabi frequencies in $n = 99$ and $n = 101$ are more than three standard deviations away from this measured value. Similar comparisons for other values of n further establish confidence that intermediate states are prepared as desired and that we can indeed transfer approximately 50% of the population to $n = 100$.

The motional superposition $|\uparrow\rangle(|0\rangle + |2\rangle)$ is straightforward to prepare by replacing the first RSB pulse by a $\pi/2$ pulse, $|\uparrow\rangle\ |0\rangle \rightarrow |\uparrow\rangle\ |0\rangle + |\downarrow\rangle\ |1\rangle$, followed by a BSB π pulse, which transforms $|\downarrow\rangle\ |1\rangle \rightarrow |\uparrow\rangle\ |2\rangle$ while not affecting $|\uparrow\rangle\ |0\rangle$ (see Fig. 1a). To realize the effective $\pi/2$ pulse $|0\rangle \rightarrow |0\rangle + |n\rangle$ when $n > 2$, after the initial RSB $\pi/2$ pulse the $|\uparrow\rangle\ |0\rangle$ component is 'shelved' with a microwave π pulse to $|\mathrm{aux}\rangle\ |0\rangle$; this state is unaltered by subsequent pairs of BSB and RSB π pulses that promote the $|\downarrow\rangle\ |k\rangle$ component to $|\downarrow\rangle\ |k+2\rangle$. The preparation is finished by a final microwave π pulse, $|\mathrm{aux}\rangle\ |0\rangle \rightarrow |\uparrow\rangle\ |0\rangle$, and a BSB pulse, $|\downarrow\rangle\ |n-1\rangle + |\uparrow\rangle\ |0\rangle \rightarrow |\uparrow\rangle(|0\rangle + |n\rangle)$, that promotes the $|\downarrow\rangle\ |n-1\rangle$ component to $|\uparrow\rangle\ |n\rangle$ while leaving the $|\uparrow\rangle\ |0\rangle$ component unaltered.

We characterize the enhanced sensitivity of each interferometer by inserting an effective 'spin-echo'-type π pulse between waiting periods of duration T and purposely induce trap-frequency changes $\Delta\omega$ with equal magnitude and opposite sign before and after the echo pulse (Fig. 1c). We use this echo technique because trap-frequency fluctuations or drifts that alter the mode frequency by approximately the same amount in both arms of the interferometer are suppressed. For the first waiting period this ideally results in an order-dependent phase of $\phi = -n\Delta\omega T$. The echo pulse is composed of the following steps: first, the pulses of the effective $\pi/2$ pulse are applied in reverse order to ideally give $|\uparrow\rangle(|0\rangle + e^{i\phi}\ |n\rangle) \rightarrow |\uparrow\rangle\ |0\rangle + e^{i\phi}\ |\downarrow\rangle\ |1\rangle$. Second, an RSB π pulse results in $e^{i\phi}\ |\uparrow\rangle\ |0\rangle + |\downarrow\rangle\ |1\rangle$, which is then walked up the number-state ladder as described for the first effective $\pi/2$ pulse. Ideally the effective echo π pulse accomplishes $|0\rangle + e^{i\phi}\ |n\rangle \rightarrow e^{i\phi}\ |0\rangle + |n\rangle$. In this way, the induced trap-frequency change of $-\Delta\omega$ during the second waiting period constructively adds to the interferometer phase $e^{i\phi}\ |0\rangle + |n\rangle \rightarrow e^{i\phi}\ |0\rangle + e^{-i\phi}\ |n\rangle$, which is transformed to $-i\sin\phi\ |\downarrow\rangle\ |1\rangle + \cos\phi\ |\uparrow\rangle\ |0\rangle$ by the final effective $\pi/2$ pulse, so the induced interferometer phase ϕ can be read out by measuring the probability to find $|\downarrow\rangle$.

We find that as we increase n in the superposition for $T = 100$ μs, the phase accumulation increases linearly with n, as expected, but—owing to accumulated imperfect state preparation steps—the contrast of the interference fringes (and therefore the fringe slope) is reduced (see Fig. 3a), reducing the signal in equation (3) of higher-order interferometers. Given this effect, we observe the highest sensitivity with the $|0\rangle + |12\rangle$ superposition state, which achieves a 17(4) dB improvement over a perfect $|0\rangle + |1\rangle$ interferometer (Fig. 3b). The $n = 12$ interferometer also performs 6.4(4) dB better (where the increase in signal-to-noise ratio has been squared, in keeping with convention) than an ideal classical interferometer (see Methods).

We can use this enhanced sensitivity to precisely track changes in the motional-mode frequency over time. We perform two Ramsey-type experiments with the phase of the final effective $\pi/2$ pulses equal to $\pm\pi/2$ so that when the pulses are resonant with the mode frequency, the

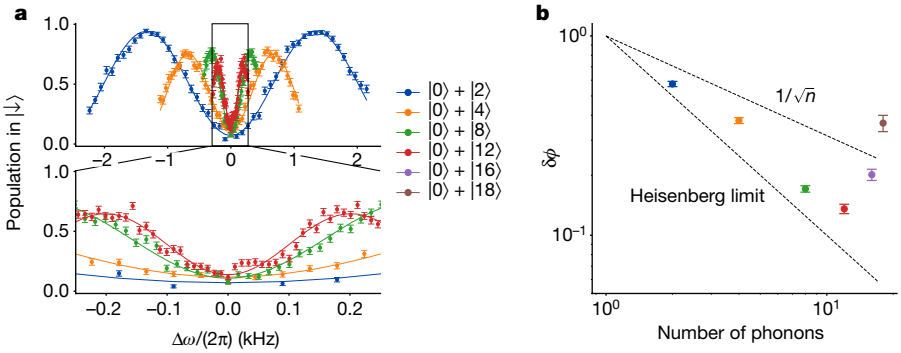

Fig. 3 | Interference and sensitivity of different number-state superpositions. a, Interference fringes for number-state interferometers with $n = 2, 4, 8, 12$. Each data point is averaged over 250 experiments and uses a waiting time of 100 μs before and after the effective π pulse. The error bars represent one standard deviation of the mean. The fringe spacing is reduced as $1/n$, as expected for Heisenberg scaling. At the same time, the fringe contrast is reduced with increasing n owing to the larger number of imperfect pulses and the higher susceptibility to mode-frequency changes, which are not stable over all of the 250 experiments for each data point. This reduces the fringe slopes for $n > 12$ below the maximal slope, which is reached for $n = 12$. Solid lines show theory fits using equation (2), with the fringe spacing, contrast and vertical offset as fit parameters. We attribute deviations from the expected sinusoidal behaviour (for example, near the centre of the $|0\rangle + |12\rangle$ fringe) to changes in the Raman sideband Rabi frequencies by a few per cent, temporarily reducing the contrast for some points. **b**, Experimentally determined noise-to-signal ratio, $\delta\phi$, as defined by equation (3), as a function of order n (dots). Also shown are theoretical lines for a perfect classical interferometer at $1/\sqrt{n}$ and the $1/n$ Heisenberg limit; this limit is valid for ideal number-state interferometers.

resulting $|\downarrow\rangle$ population from each Ramsey experiment is ideally 1/2. A difference between the populations for the $+\pi/2$ and $-\pi/2$ cases provides an error signal that we feed back to the local oscillator to follow the fringe pattern as the mode-frequency drifts owing to changes in stray electric fields and the sources providing the electrode potentials.

This procedure is complicated by the fact that the sideband transition frequencies are shifted by the a.c. Stark effect from the Raman beams. These result in phases beyond those described by equation (1) that shift the interferometer fringes. To mitigate this effect, as well as to subtract non-zero phase accumulation during the creation of the superposition state, we use auto-balanced Ramsey spectroscopy[30] (see Methods). Instead of using two Ramsey experiments that provide the error signal that is fed back to the pulse frequency, we interleave four Ramsey experiments with two different Ramsey times, T_{short} and T_{long} (typically 20 μs and 100 μs, respectively). The phase between the two $\pi/2$ pulses is adjusted to compensate for systematic phases according to the error signal obtained from the short-pulse Ramsey experiments, and the frequency of the local oscillator is adjusted according to that from the long-pulse Ramsey experiments. These phase and frequency adjustments are applied equally to both the short- and long-pulse Ramsey experiments. This suppresses all contributions to phase accumulation other than the phase difference accumulated owing to the different free-precession times, which is unperturbed by laser beam couplings[30].

When tracking the mode frequency in this way, we can record the frequency error versus time for different-n interferometers. We can then determine the overlapping Allan deviation[31] as a function of the averaging interval and compare it for the different interferometers (Fig. 4a). The data shown in Fig. 4a were taken while interleaving experiments performed with the $|0\rangle + |2\rangle$, $|0\rangle + |4\rangle$, $|0\rangle + |6\rangle$ and $|0\rangle + |8\rangle$ interferometers to allow a direct comparison of their sensitivity under the same noise and drift conditions. For long averaging periods, trap-frequency drifts dominate the uncertainty. As expected, this gives the same asymptotic long-time slope of the Allan deviation for all interferometers. Importantly, the increased sensitivity of higher-n interferometers reduces the time interval required to average down to a certain level for n up to 8. For the $n = 8$ interferometer, we observe

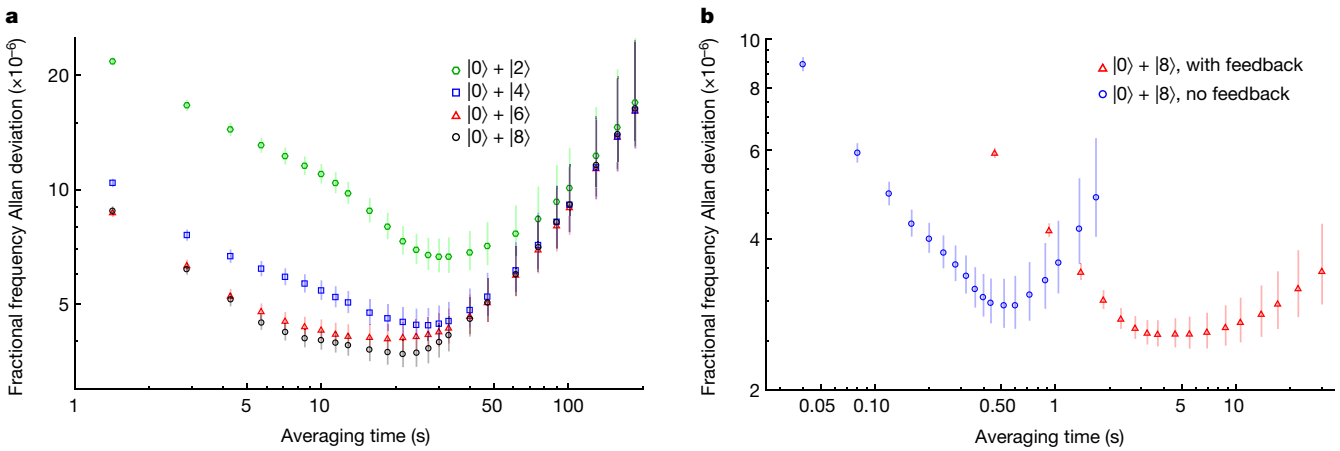

Fig. 4 | Tracking of oscillator frequency using number-state interferometers. a, Allan standard deviation of tracked fractional trap frequencies versus averaging time for interleaved experiments with $n = 2$, $n = 4$, $n = 6$ and $n = 8$ interferometers . The repetition rate of a single run, comprising long (100 μs Ramsey time) and short (20 μs Ramsey time) auto-balance sequences on both sides of the fringe was approximately 7 s^{-1}. The $n = 8$ interferometer produces the lowest Allan deviation of the fractional frequency. Trap-frequency drifts begin to dominate the Allan deviation at tens of seconds. **b**, Uncertainty of the fractional mode frequency versus averaging time for two series of only $n = 8$ interferometer runs performed to maximize the measurement duty cycle. We achieve a minimal fractional-frequency Allan deviation of $2.6(2) \times 10^{-6}$ at approximately 4 s of averaging time with tracking activated (red triangles) and an experiment rate of approximately 43 s^{-1} as defined above. The Allan standard deviation for averaging times of up to 1 s, without tracking activated, is shown by the blue circles. The minimum is reached after 0.5 s, with the experiment rate increased to approximately 250 s^{-1}. The error bars represent one standard deviation of the mean.

the minimum Allan standard deviation at approximately 23 s of averaging in this interleaved-experiment comparison. By running only the $n = 8$ interferometer sequences, we increase the measurement duty cycle, which accelerates the rate with which the Allan deviation approaches its minimum. Under these conditions, the minimal fractional frequency Allan deviation of $2.6(2) \times 10^{-6}$ (about 19 Hz at 7.2 MHz) is reached at approximately 4 s of averaging (red triangles in Fig. 4b). To further increase the measurement rate, we record the population differences determined in all four Ramsey experiments comprising the auto-balance sequence without feeding back on the local oscillator frequency. This eliminates the latency due to computer control of the frequency tracking. As long as the populations of the four Ramsey experiments determine the frequency change uniquely, we can run a series of $n = 8$ interferometer experiments (each taking 4 ms) without feedback to shorten the time required to reach the minimum of $2.9(4) \times 10^{-6}$ to approximately 0.5 s, before the uncompensated mode-frequency drift produces an increasing Allan deviation (Fig. 4b, blue circles). Although the minimum value of the Allan deviation is not lower when taking data in this fashion compared to when tracking the drift, this experiment gives an idea of how quickly we could average down to a few parts in 10^{-6} if the tracking latency is minimized.

In conclusion, we have demonstrated the preparation of approximate number states up to $n = 100$ for the harmonic motion of a trapped ion, and characterized the quantum-enhanced sensitivity of number-state interferometers up to $n = 18$. We used this sensitivity to measure the mode frequency with a minimum fractional frequency uncertainty of $2.6(2) \times 10^{-6}$. The quantum advantages of our method were limited by imperfections in state preparation and detection, as well as by uncontrolled mode-frequency changes, which are probably caused by time-varying stray fields and technical noise on the potentials applied to trap electrodes (see Methods). As an extension of the work presented here, it should be possible to observe such mode-frequency noise during free precession by refocusing with one or more effective π pulses. This would allow us to filter the response of the ion to certain spectral components of the motional mode-frequency noise, providing a quantum lock-in analyser, in analogy to characterizations of magnetic-field noise with a trapped ion[32]. By using number-state superpositions, we can transfer the quantum advantage reported here to achieve 'quantum gain' in such lock-in measurements.

More generally, we expect that the techniques demonstrated here, as well as alternative approaches[33,34], can be applied to characterize other harmonic oscillators in the quantum regime (as in ref. [35]) with increased precision and on timescales that were previously inaccessible. Such capabilities could support quantum metrology and improve the prospects of fault-tolerant quantum information processing, where some of the most advanced experimental platforms are limited by harmonic oscillator coherence.

Online content

Any methods, additional references, Nature Research reporting summaries, source data, statements of code and data availability and associated accession codes are available at https://doi.org/10.1038/s41586-019-1421-y.

Received: 30 July 2018; Accepted: 5 June 2019;
Published online 22 July 2019.

1. Pezzè, L., Smerzi, A., Oberthaler, M. K., Schmied, R. & Treutlein, P. Quantum metrology with nonclassical states of atomic ensembles. *Rev. Mod. Phys.* **90**, 035005 (2018).
2. Braun, D. et al. Quantum-enhanced measurements without entanglement. *Rev. Mod. Phys.* **90**, 035006 (2018).
3. Caves, C. M., Thorne, K. S., Drever, R. W. P., Sandberg, V. D. & Zimmermann, M. On the measurement of a weak classical force coupled to a quantum-mechanical oscillator. I. Issues of principle. *Rev. Mod. Phys.* **52**, 341–392 (1980).
4. Boto, A. N. et al. Quantum interferometric optical lithography: exploiting entanglement to beat the diffraction limit. *Phys. Rev. Lett.* **85**, 2733–2736 (2000).
5. Haroche, S. & Raymond, J.-M. *Exploring the Quantum* (Oxford University Press, 2006).
6. Schrödinger, E. Der stetige Übergang von der Mikro- zur Makromechanik. *Naturwissenschaften* **14**, 664–666 (1926).
7. Glauber, R. J. Nobel lecture: one hundred years of light quanta. *Rev. Mod. Phys.* **78**, 1267–1278 (2006).
8. Margolus, N. & Levitin, L. B. The maximum speed of dynamical evolution. *Physica D* **120**, 188–195 (1998).
9. Caves, C. M. & Shaji, A. Quantum-circuit guide to optical and atomic interferometry. *Opt. Commun.* **283**, 695–712 (2010).
10. Meekhof, D. M., Monroe, C., King, B. E., Itano, W. M. & Wineland, D. J. Generation of nonclassical motional states of a trapped atom. *Phys. Rev. Lett.* **77**, 2346 (1996).
11. Ballance, C. J., Harty, T. P., Linke, N. M., Sepiol, M. A. & Lucas, D. M. High-fidelity quantum logic gates using trapped-ion hyperfine qubits. *Phys. Rev. Lett.* **117**, 060504 (2016).
12. Gaebler, J. P. et al. High-fidelity universal gate set for $^{9}Be^{+}$ ion qubits. *Phys. Rev. Lett.* **117**, 060505 (2016).
13. Blais, A., Huang, R.-S., Wallraff, A., Girvin, S. M. & Schoelkopf, R. J. Cavity quantum electrodynamics for superconducting electrical circuits: an architecture for quantum computation. *Phys. Rev. A* **69**, 062320 (2004).
14. Aspelmeyer, M., Kippenberg, T. & Marquardt, F. Cavity optomechanics. *Rev. Mod. Phys.* **86**, 1391–1452 (2014).
15. Grimm, R., Weidemüller, M. & Ovchinnikov, Y. B. Optical dipole traps for neutral atoms. *42 Adv. Atom. Mol. Opt. Phys.* 95–170 (2000).
16. Leibfried, D., Blatt, R., Monroe, C. & Wineland, D. J. Quantum dynamics of single trapped ions. *Rev. Mod. Phys.* **75**, 281–324 (2003).
17. Aasi, J. et al. Enhanced sensitivity of the LIGO gravitational wave detector by using squeezed states of light. *Nat. Photon.* **7**, 613–619 (2013).
18. Ladd, T. D. et al. Quantum computers. *Nature* **464**, 45–53 (2010).
19. Wineland, D. J., Bollinger, J. J. & Itano, W. M. Laser fluorescence mass spectroscopy. *Phys. Rev. Lett.* **50**, 628–631 (1983).
20. Sheridan, K. & Keller, M. Weighing of trapped ion crystals and its applications. *New J. Phys.* **13**, 123002 (2011).
21. Alonso, J. et al. Generation of large coherent states by bang–bang control of a trapped-ion oscillator. *Nat. Commun.* **7**, 11243 (2016).
22. Home, J. P., Hanneke, D., Jost, J. D., Leibfried, D. & Wineland, D. J. Normal modes of trapped ions in the presence of anharmonic trap potentials. *New J. Phys.* **13**, 073026 (2011).
23. Leibfried, D. et al. Trapped-ion quantum simulator: experimental application to nonlinear interferometers. *Phys. Rev. Lett.* **89**, 247901 (2002).
24. Cirac, J. I. & Zoller, P. Quantum computations with cold trapped ions. *Phys. Rev. Lett.* **74**, 4091–4094 (1995).
25. Brownnutt, M., Kumph, M., Rabl, P. & Blatt, R. Ion-trap measurements of electric-field noise near surfaces. *Rev. Mod. Phys.* **87**, 1419–1482 (2015).
26. Itano, W. M. et al. Quantum projection noise: population fluctuations in two-level systems. *Phys. Rev. A* **47**, 3554–3570 (1993).
27. Monroe, C., Meekhof, D. M., King, B. & Wineland, D. J. A "Schrödinger cat" superposition state of an atom. *Science* **272**, 1131–1136 (1996).
28. Wilson, A. C. et al. Tunable spin–spin interactions and entanglement of ions in separate potential wells. *Nature* **512**, 57–60 (2014).
29. Monroe, C. et al. Resolved-sideband Raman cooling of a bound atom to the 3D zero-point energy. *Phys. Rev. Lett.* **75**, 4011–4014 (1995).
30. Sanner, C., Huntemann, N., Lange, R., Tamm, C. & Peik, E. Autobalanced Ramsey spectroscopy. *Phys. Rev. Lett.* **120**, 053602 (2018).
31. Howe, D. A., Allan, D. U. & Barnes, J. A. Properties of signal sources and measurement methods. In *Proc. 1981 Freq. Cont. Symp.* 1–47 (IEEE, 1981).
32. Kotler, S., Akerman, N., Glickman, Y., Keselman, A. & Ozeri, R. Single-ion quantum lock-in amplifier. *Nature* **473**, 61–65 (2011).
33. Ziesel, F. et al. Experimental creation and analysis of displaced number states. *J. Phys. At. Mol. Opt. Phys.* **46**, 104008 (2013).
34. Wolf, F. et al. Motional Fock states for quantum-enhanced amplitude and phase measurements with trapped ions. Preprint at https://arxiv.org/abs/1807.01875 (2018).
35. Chu, Y. et al. Creation and control of multi-phonon Fock states in a bulk acoustic-wave resonator. *Nature* **563**, 666–670 (2018).

Acknowledgements We thank D. Allcock, D. Slichter and R. Srinivas for discussions and assistance with the experimental setup, and H. F. Leopardi and H. Knaack for comments on the manuscript. This work was supported by IARPA, ARO, ONR and the NIST Quantum Information Program. K.C.M. acknowledges support by an ARO QuaCGR fellowship through grant W911NF-14-1-0079. J.K. acknowledges support by the Alexander von Humboldt foundation.

Author contributions K.C.M. and D.L. conceived the experiments, carried out the measurements, analysed the data and wrote the main part of the manuscript. K.C.M., J.K., S.C.B. and A.C.W. built and maintained the experimental setup. D.J.W., A.C.W. and D.L. developed parts of the experimental setup and supervised the work. All authors discussed the results and contributed to the manuscript.

Competing interests The authors declare no competing interests.

Additional information
Extended data is available for this paper at https://doi.org/10.1038/s41586-019-1421-y.
Reprints and permissions information is available at http://www.nature.com/reprints.
Correspondence and requests for materials should be addressed to K.C.M.
Publisher's note: Springer Nature remains neutral with regard to jurisdictional claims in published maps and institutional affiliations.

METHODS

Precision limit of 'classical' measurements on 'classical' states. There is almost general agreement in the literature that any 'classical' limit to measurement precision on the frequency of a harmonic oscillator will be proportional to $\sqrt{\bar{n}}$, where $\bar{n}$ is the average occupation number[2]. However, there is no general agreement on the pre-factor to that scaling, which is necessary to fully define a "standard quantum limit"[2]. The limit that we establish assumes an observer with classical resources (defined below) that are perfectly implemented.

To compare our experiments to a well defined classical reference experiment, we extend the notions of classical experiments with light fields given by R. J. Glauber[7] to a general harmonic oscillator. For light fields, R. J. Glauber restricted classical sources to coherent light. In this spirit, we broaden the possible physical implementations of R. J. Glauber's discussion to any system that can be described as a harmonic oscillator but limit the admissible operations to coherent displacements. Harmonic oscillator quantum observables are expressed with the ladder operators $\hat{a}$ and $\hat{a}^\dagger$, and a coherent state is an eigenstate of the annihilation operator with $\hat{a}\ |\alpha\rangle = \alpha\ |\alpha\rangle$. The oscillator's average number of quanta is then given by the expectation value $\bar{n}$ of the number operator $\bar{n} = \langle\alpha\ |\hat{a}^\dagger\hat{a}|\ \alpha\rangle = |\alpha|^2$. R. J. Glauber restricted classical measurements to measuring intensities for light fields (for example, the intensities arising on a screen owing to the interference of the two light fields from a double-slit arrangement). We generalize light-field intensity to number expectation values $\bar{n}$ as the permitted classical measurements in a harmonic oscillator. The attainable signal-to-noise ratio of such measurements will be limited by shot noise, which is given by the standard deviation of a Poisson distribution with mean $\bar{n}$, $\Delta P_{\bar{n}} = \sqrt{\bar{n}}$, for an ideal measurement on a coherent state with unit quantum efficiency and no excess noise. To compare to number-state superpositions of the form $|\Psi_n\rangle = |0\rangle + |n\rangle$, we require that the classical interferometer uses no more energy than the competing number-state interferometer, $\bar{n} = \langle\Psi_n|\hat{a}^\dagger\hat{a}|\Psi_n\rangle \leq n$. This definition of equal resources is somewhat arbitrary, for example, one could also argue for the same maximal energy. However, the coherent states have no well defined maximal energy, and it is always possible to rescale from our definition to another definition of equal resources. The scaling factor would probably be of order unity in most cases and, irrespective of its value, the ideal non-classical interferometer will eventually outperform its classical counterpart owing to its more favourable scaling in $\bar{n}$.

With the definitions above, we can devise an interferometer experiment that has the salient features of a Ramsey experiment but is based on classical states and measurements. A Ramsey experiment consists of two excitations with known relative phase, separated by 'free precession' of duration T. An example of a classical-like Ramsey experiment could be to send an radiofrequency pulse from a reference oscillator with known frequency and phase into a near-resonant circuit. The pulse will drive oscillations in the circuit, which then evolves freely for T. A second pulse is then sent to the circuit and—depending on its phase relative to the first pulse, and the phase that the excitation has picked up in the resonant circuit during T—the two pulses interfere constructively to further build up the field in the circuit or interfere destructively, diminishing the circuit excitation. For a general harmonic oscillator, this can conveniently be described in phase space in a frame oscillating at the frequency of the reference oscillator. Starting in the ground state, the first excitation creates a coherent state $|\alpha_1\rangle$, where we can choose phase space coordinates that make $\alpha_1 \geq 0$ real without losing generality. During the free-precession time T, the state picks up a phase of ϕ_T, which transforms it to $|\alpha_1\rangle_T = |\alpha_1\exp(i\phi_T)\rangle$. In analogy to a Ramsey experiment, the second excitation is chosen to have the same magnitude with phase ϕ relative to the first excitation, $\alpha_2 = \alpha_1\exp(i\phi)$. This transforms the state (up to a global phase that is of no consequence to this experiment) into $|\alpha_1\rangle_T = |\alpha_1\{1+\exp[i(\phi_T-\phi)]\}\rangle$. Following R. J. Glauber's definition of classical measurements, we measure the average occupation $\bar{n}$

$$\bar{n} = 4{\alpha_1}^2\left[\frac{1}{2}+\frac{1}{2}\cos(\phi-\phi_T)\right] \tag{4}$$

For a fair comparison to a number-state superposition $|0\rangle + |n\rangle$, we would like to restrict our resources to $\bar{n} \leq n$ for all possible ϕ and ϕ_T, so we choose the maximum value, $4{\alpha_1}^2 = n$. Under this restriction, we recover a classical version of the Ramsey fringes described by equation (2), where we measure $\bar{n} = 0$ when $\phi - \phi_T = (2m+1)\pi$ and $\bar{n} = n$ when $\phi - \phi_T = 2m\pi$, with m an integer. We want to minimize the noise-to-signal ratio that equation (3) restricted to coherent excitations and to a small free-precession phase $|\phi_T| \approx 0 \ll \pi$. This noise-to-signal ratio is

$$\delta\phi_c = \frac{\Delta P_{\bar{n}}}{|\partial P_{\bar{n}}/\partial\phi_T|}\bigg|_{\phi_T=0} = \frac{\sqrt{n\left(\frac{1}{2}+\frac{1}{2}\cos\phi\right)}}{\frac{n}{2}\sin\phi} = \sqrt{\frac{1}{n}}\sqrt{\frac{1+\frac{1}{\cos^2\phi}}{2}} \tag{5}$$

This occurs when $\phi = \pi$, which describes two equal and opposite displacements that put the harmonic oscillator back to the vacuum state if the free-precession phase is $\phi_T = 0$. Both the noise and the signal vanish for this interferometer in such a way that their ratio stays finite at $\delta\phi_c = 1/\sqrt{n}$.

This is the best one can do in the case of no excess noise in the system. In practice, when some added noise would be present, we would choose a value of ϕ that maximizes the signal, as we did for the case of the number-state interferometer. In this case (as was also true for the number-state interferometer), the point of maximal signal occurs for $\phi = \pi/2$, so the practical noise-to-signal-ratio yields

$$\delta\phi_p = \frac{\sqrt{n\left(\frac{1}{2}+\frac{1}{2}\cos\phi\right)}}{\frac{n}{2}\sin\phi}\bigg|_{\phi=\pi/2} = \sqrt{\frac{2}{n}} \tag{6}$$

This interferometer has no practical drawbacks, optimally suppresses additional noise and leads to an increase of the noise-to-signal over the optimal value by $\sqrt{2}$. This implies that the advantage of a number-state interferometer may increase by $\sqrt{2}$ over the ideal limit in a realistic setting, where excess noise (such as current noise or dark counts of a detector) is almost inevitable. This also is arguably a more direct comparison to the $|0\rangle + |n\rangle$ interferometer experiment, where we choose the same relative phase of $\phi = \pi/2$ between the two pulses to maximize the signal. Despite the case to be made for using the more practical limit in our comparisons, we strictly use the more stringent ideal classical interferometer in all of our sensitivity comparisons of the number-state interferometers in the main text.

Experimental details. *Experimental improvements since initial demonstration.* The techniques used for producing non-classical states of motion were initially demonstrated in ref. [10]. Since then, many improvements have been made to our apparatus to allow us to achieve high-fidelity production and control of number states with $n > 16$. The most notable of these changes for its contribution to this work has been stabilizing the intensity of the Raman beams on the ion. This has been achieved by replacing dye lasers with much less noisy fibre lasers that reduce intensity fluctuations of the beams[36], the use of recently developed ultraviolet photonic crystal fibres[37] to mitigate beam-pointing fluctuations, and rigid mechanical supports to better mechanically register the trap to the optical table, which additionally mitigates beam-pointing fluctuations on the ion. We have also reduced the heating rate of the trap used in our experiments by one order of magnitude, to 17 quanta per second, compared to experiments in ref. [23], where this rate was approximately 170 quanta per second. This reduction in heating rate, while the ion is closer to the nearest electrode surface (approximately 40 μm, as opposed to 270 μm)[23] is partially due to cooling of the electrode traps to 4 K inside a bath cryostat.

Timescales of experiments. For all of the experiments described in this paper, the state preparation consists of Doppler cooling (about 120 μs) followed by ground-state cooling (about 110 μs) and a microwave carrier π pulse $|\downarrow\rangle \rightarrow |\uparrow\rangle$ (about 5 μs). At the end of each experiment, a 400-μs detection pulse on the cycling transition is applied. The duration of the Raman RSB $|\uparrow\rangle\ |0\rangle \rightarrow |\downarrow\rangle\ |1\rangle$ π pulse which sets the Rabi frequency $\Omega_{0,1}$, is approximately 13 μs, so the duration of individual experiments can be calculated by using $\Omega_{0,1}$ as a 'base' unit to calculate the times of sideband π pulses for higher n values according to[16]

$$\frac{\Omega_{n,n+s}}{\Omega_{0,1}} = \eta^{|s|-1}\sqrt{\frac{n_<!}{n_>!}}L_{n_<}^{|s|}(\eta^2) \tag{7}$$

where $L_n^{|s|}$ is the generalized Laguerre polynomial and $n_>$ ($n_<$) is the greater (smaller) of $n+s$ and n (see also Fig. 2d). We can then sum the durations of the individual sideband pulses (and, in the case of the superposition states, the durations of the ~5-μs microwave $|\uparrow\rangle \rightarrow |\text{aux}\rangle$ π pulses) used. Extended Data Table 1 lists the durations of the sequences used to generate pure number states and number-state superpositions. It is possible to substantially decrease these durations, as long as the sidebands are still resolved.

The sidebands in our interferometers rely on the same Raman laser coupling that is used in most two-qubit gates, so the timescale for a single BSB or RSB pulse is of the same order as a typical gate time. This limits the usefulness of the demonstrated frequency tracking method for improving gate fidelity, but interferometric tracking would certainly help with longer-term drifts and would reduce the time required to measure the trap frequency with a certain precision.

Sources of decoherence. At the 7.2-MHz axial-mode frequency, the heating rate is relatively low, approximately 17 quanta per second. Consequently, the dominant source of decoherence in these experiments is dephasing due to fluctuations in the mode frequency. These fluctuations probably arise from technical noise from the voltage source, uncontrolled charging from stray light scattering off the dielectric material between the trap electrodes, and amplitude instabilities in the radiofrequency source that generates the pseudo-potential. We also attribute longer timescale drift (of the order of minutes to hours, and with a magnitude of about

$1-10\ \mathrm{Hz\ s^{-1}}$) to uncontrolled charging and discharging. This charging affects mode-frequency-tracking experiments and leads to unpredictable deviations from the ideal white-noise $1/\sqrt{\tau}$ scaling with averaging time τ during experimental runs to determine Allan variances. A more detailed investigation of this noise and of ways to further suppress it is currently in progress in our laboratory.

Auto-balanced frequency-tracking experiments. The auto-balanced sequence (see Extended Data Fig. 1) for mode-frequency tracking comprises four interleaved Ramsey experiments, two each with Ramsey times t_{short} and t_{long}, where the phase of the second effective $\pi/2$ pulse is $+\pi/2$ relative to the first $\pi/2$ pulse for one of the experiments and $-\pi/2$ for the other. For a given Ramsey time, the two experiments with $+\pi/2$ and $-\pi/2$ relative phase interrogate the fringe close to its largest positive and negative slope, respectively. If the long-pulse Ramsey experiments are exactly on resonance, both should result in the same average population in $|\downarrow\rangle$, so the signal difference is zero on average. If the Ramsey experiment is off-resonance, the signal difference provides a non-zero error signal p_{long}, which is used to calculate the offset $\delta\omega$ between the assumed mode frequency ω_{a} and the actual mode frequency. The offset $\delta\omega$ is fed back to the local oscillator (LO), which updates its frequency to $\omega = \omega_{\mathrm{a}} + \delta\omega$. This in turn updates the frequency of the BSB and RSB pulses to $\omega_{\mathrm{LO}} = \omega_0 + \omega_{\mathrm{a}} + \delta\omega$ and $\omega_{\mathrm{LO}} = \omega_0 - \omega_{\mathrm{a}} - \delta\omega$, respectively, where $\hbar\omega_0$ is the energy difference between $|\uparrow\rangle$ and $|\downarrow\rangle$, as described in the main text ($\hbar$, reduced Planck constant). The short-pulse Ramsey experiments provide an error signal of p_{short}, as described above, which is now used to compute a phase offset $\delta\phi$ that is added to the relative phase between the two effective π pulses, $\phi_{\mathrm{LO}} = \pm\pi/2 + \delta\phi$. Feedback on this phase reduces 'frequency pulling' due to non-zero phase accumulation during the pulses, which can be caused by slowly drifting, pulse-synchronous systematic errors such as a.c. Stark shifts[30]. For a more detailed description of the auto-balanced Ramsey technique, see ref. [30].

Anharmonic contributions. We do not expect the anharmonicity of the trapping potential to be a considerable limitation or source of systematic error. Previous calculations[22] for a similar trap and estimates based on a numerical simulation of our current trap predict an anharmonic component of a few parts in 10^{-7} per quantum on the axial-mode frequency. With a maximal superposition state of $|0\rangle + |8\rangle$ used in the mode-tracking experiments, this would cause an offset of about 1×10^{-6}, which is within the minimum measurement uncertainty.

Data availability

The datasets generated or analysed during the current study are available from the corresponding author on reasonable request.

36. Wilson, A. C. et al. A 750 mW, continuous-wave, solid-state laser source at 313 nm for cooling and manipulating trapped $^{9}Be^{+}$ ions. *Appl. Phys. B* **105**, 741–748 (2011).
37. Colombe, Y., Slichter, D. H., Wilson, A. C., Leibfried, D. & Wineland, D. J. Single-mode optical fiber for high-power, low-loss UV transmission. *Opt. Express* **22**, 19783–19793 (2014).

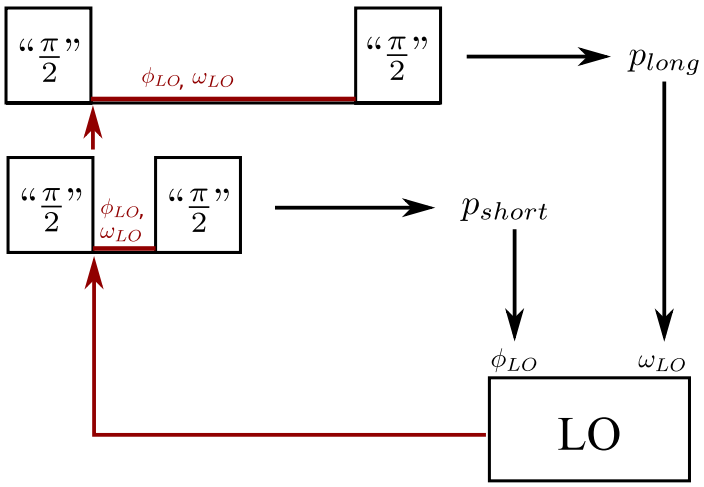

Extended Data Fig. 1 | Schematic illustrating the auto-balanced feedback loop. The feedback is applied to the LO, a frequency source used as a reference to compare to the ion's oscillation frequency. The LO controls the phases and frequencies of the BSB and RSB laser pulses (see Fig. 1a) during the mode-frequency tracking experiments. The difference between the populations measured after a pair of Ramsey experiments with long waiting times provides an error signal, p_{long}, which is used to feed back on the LO frequency, ω_{LO}. Similarly, a second pair of Ramsey experiments with short waiting times provides and error signal, p_{short}, which is used to feed back on an additional LO phase offset ϕ_{LO} between the first and second effective π/2-pulses ("π/2"). The long- and short-waiting-time Ramsey experiments are interleaved, with ϕ_{LO} and ω_{LO} applied equally to both. For more details on auto-balanced Ramsey experiments, see ref. [30].

Extended Data Table 1 | Duration of pulse sequences used to produce number states and number-state superpositions

n	$\mathrm{T}(\lvert n\rangle)$ (μs)	$\mathrm{T}(\lvert 0\rangle + \lvert n\rangle)$ (μs)
2	22	16
4	38	41
6	51	54
8	63	66
12	86	89
16	109	112
20	133	–
40	196	–
80	293	–
100	335	–

These values are for a base Rabi frequency of $\Omega_{0,1} = \pi/(13\ \mu\mathrm{s})$. Beyond $n = 40$, we use higher-order sidebands, which allows us to use transitions with higher Rabi frequencies and skip 'rungs' as we move the ion up the number-state ladder.